Submitted to the XXIX International Rochester Conference on High Energy Physics, Vancouver, Canada, July 1998

Precision Measurement of the Inclusive Deep Inelastic *ep* Scattering Cross Section at Low Q^2

H1 Collaboration

Abstract:

A measurement of the deep inelastic scattering cross section is reported for momentum transfers squared $2 \leq Q^2 \leq 120$ GeV^2 and for Bjorken-x values $3 \cdot 10^{-5} < x < 0.1$. The data were collected by the HERA experiment H1 in 1997, with a luminosity of 15 pb^{-1} for $Q^2 > 10$ GeV^2 and of 2 pb^{-1} taken in a dedicated run for Q^2 below 10 GeV^2. This measurement is by nearly a factor of two more accurate than results presented previously and it uses in the lower Q^2 region the new Backward Silicon Tracker of the H1 experiment. A QCD analysis of the cross section data combined with fixed target experiments shows theory to NLO to be in very good agreement with the new data. A novel technique has been developed to determine the longitudinal structure function $F_L(x, Q^2)$ using the measured derivative $\partial\sigma/\partial \log y$. This permitted to access F_L down to low Q^2 values of 3 GeV^2 and lead to results consistent with the method previously used to extract $F_L(x, Q^2)$ at larger Q^2.

Abstract 534
Parallel Session 4
Plenary Session 6

1 Introduction

The measurement of the inclusive neutral current deep inelastic scattering (DIS) cross section $\sigma(ep \to eX)$ has been one of the prime tasks at HERA. Its precise determination is required in the accessible kinematic range for the understanding of proton substructure and precision tests of QCD. A new, preliminary, result is presented here based on data taken with the H1 detector in 1997 comprising two samples:

- For momentum transfers squared $Q^2 > 10$ GeV^2 the full data taken in the year 1997 has been analyzed using a luminosity of 15 pb^{-1}. The acceptance of the backward apparatus with the calorimeter SPACAL and the planar drift chamber BDC extends to $Q^2 \leq 120$ GeV^2. Very large values of the inelasticity variable $y = Q^2/sx$ are reached in the acceptance region of the central jet drift chamber (CJC) which permits subtraction of the photoproduction background using the measured charge of the scattered positron candidate. Here x is the Bjorken scale variable and s is the centre of mass energy $s = 4E_eE_p$ determined by the positron and proton beam energies E_e and E_p.

- For $2 \leq Q^2 < 10$ GeV^2 a data sample with a luminosity of 2 pb^{-1} was collected in a dedicated run using minimum bias triggers at the end of the 1997 running period. The measurement accuracy was improved and its range extended towards low values of y in the acceptance region of the backward silicon tracker (BST) which has been used for the first time in the inclusive cross section measurement for track and vertex reconstruction and for photoproduction background rejection.

This paper describes the analysis of the new data which leads to a number of results presented here:

- The deep inelastic scattering cross section is measured with a statistical precision of about 1%. The systematic uncertainty has reached a new level of accuracy with values between about 3% and 4% in the bulk region of this data which are compared with the previous H1 measurements [1–4].

- The improved accuracy permits a new analysis of the proton structure function $F_2(x, Q^2)$ and of the DIS cross section using NLO QCD and including data of the muon-nucleon fixed target experiments and also the preliminary high $Q^2 \geq 200$ GeV^2 cross section data recently released by H1 [5].

- The data has been used to measure at fixed Q^2 the derivative of the reduced cross section σ_r, $\partial\sigma/\partial \log y$, which is determined accurately due to the large data statistics and cancellation of systematic effects.

- Using this cross section derivative data a novel method is introduced to access at large y the longitudinal structure function $F_L(x, Q^2)$ extending its determination to the region of low Q^2.

The paper is organized as follows. Section 2 describes the cross section measurement, i.e. the DIS kinematics, the H1 detector, the event selection and simulation, and the resulting cross section data. In Section 3 the QCD analysis is presented. Section 4 discusses the high y cross section measurement and the results on the extraction of the longitudinal structure function. A short summary is given in Section 5.

2 Cross Section Measurement

2.1 Kinematics

In 1997 HERA was operated with positrons of energy $E_e = 27.5$ GeV and protons of energy $E_p = 820$ GeV. The event kinematics were reconstructed using the energy of the scattered positron E'_e and the polar angle θ_e according to the relations

$$Q^2_e = \frac{E'^2_e \sin^2\theta_e}{1-y_e} \qquad\qquad y_e = 1 - \frac{E'_e}{E_e}\ \sin^2(\theta_e/2). \tag{1}$$

Here θ_e is defined with respect to the proton beam direction, defining the z axis.

The measurement of the hadronic final state determines the inelasticity variable y to be [6]

$$y_h = \frac{\sum_i(E_i - p_{z,i})}{2E_e} = \frac{\sum_h}{2E_e}, \tag{2}$$

where E_i and $p_{z,i}$ are the energy and longitudinal momentum component of a final state particle i, the masses being neglected. In this analysis the kinematics was reconstructed with the lepton variables Q^2_e and y_e and also using the so-called Σ variables defined as

$$Q^2_\Sigma = \frac{E'^2_e \sin^2\theta_e}{1-y_\Sigma} \qquad\qquad y_\Sigma = \frac{y_h}{1+y_h-y_e} = \frac{\sum_h}{\sum_h + E'_e(1-cos\theta_e)}. \tag{3}$$

The y_h and y_Σ variables can be measured down to low y, and y_Σ is less sensitive to initial state radiation since in Eq.3 the initial energy E_e is calculated using the total secondary energy reconstructed in the detector [7]. The Bjorken x variable is calculated as Q^2/sy.

The reconstruction of the event kinematics permits the so-called reduced DIS scattering cross section to be determined which in the notation of [8] is defined as

$$\frac{Q^4 x}{2\pi\alpha^2 Y_+}\cdot\frac{d^2\sigma}{dxdQ^2} = \sigma_r = F_2(x,Q^2) - \frac{y^2}{Y_+}\cdot F_L(x,Q^2) \tag{4}$$

with $Y_+ = 1 + (1-y)^2$. The cross section σ_r, for $Q^2 << M^2_Z$, is given by the two proton structure functions $F_2(x,Q^2)$ and $F_L(x,Q^2)$ which are related by $0 \le F_L \le F_2$. Thus the contribution of F_L is suppressed in most of the kinematic range explored by the HERA experiments and approximately the relation $\sigma_r = F_2$ holds with the exception of the high y region.

2.2 H1 Detector

The H1 detector [9] is a nearly hermetic apparatus with a solenoidal magnetic field of 1.15 T built to investigate high-energy ep interactions at HERA. For polar angles $\theta_e > 153^o$ the scattered positron energy E'_e is measured in the backward electromagnetic lead-fibre calorimeter (SPACAL [10]) which has an integrated timing function to veto proton beam induced background interactions. Identification of the scattered positron and the polar angle measurement make use of a backward drift chamber (BDC) and a backward silicon strip detector (BST) situated in front of the SPACAL.

The BST [11], in its 1997 configuration, is a 4 plane silicon strip detector telescope with 64 wedge shaped, single sided, double metal detectors having p^+ strips of 96 μm readout pitch arranged concentric around the beam axis to measure the polar angle of crossing tracks for θ between 172^o and 177^o.

The hadronic final state was reconstructed with the Liquid Argon (LAr) calorimeter, the tracking detectors and the SPACAL. The interaction vertex was determined with the central drift chambers: the jet chamber CJC and the two z drift chambers. The vertex determination is complemented at large Q^2 by the inner proportional chamber CIP and at low Q^2 by the silicon tracker. This largely enhances the vertex reconstruction efficiency at low y where the scattered positron has to define the vertex.

The luminosity was determined from the cross section of the elastic bremsstrahlung process, measured with a precision of 1.5% using the method outlined in [12]. The final state photon and the positron scattered at very low Q^2 can be detected in calorimeters ("electron and photon taggers") which are situated close to the beam pipe at distances of 33 m and 103 m from the interaction point in the positron beam direction. The luminosity measurement was by about 7% corrected for the occurence of late and early proton beam satellites which do not enter the selected data sample.

Part of the photoproduction background events is recognized by tagging the scattered positron in the electron tagger calorimeters upstream the positron beam. This tagged event sample has been essential to understand the background due to very low Q^2 processes.

2.3 Event Selection and Simulation

The data are triggered using the local energy sums in the SPACAL calorimeter with an energy threshold set to 6 GeV in the large data sample. This was lowered to 5 GeV in the dedicated low Q^2 run. A trigger down to 2 GeV has been realized by requiring in addition a minimum radius of the accepted cluster position in the SPACAL and a valid vertex trigger signature in the proportional chamber system. These requirements reduced the low energy background to a tolerable level. In the dedicated low Q^2 run the minimum radius cut, applied at the second trigger level, was relaxed from about 30 cm in the nominal 1997 data taking to 15 cm. The efficiency of all trigger elements was larger than 96% and controlled by independent tracking triggers to an accuracy of 0.5% degrading to 1% at lowest energies.

The event selection criteria are summarized in table 1. For the large $Q^2 > 10$ GeV^2 sample the scattered positron was identified as the cluster with maximum transverse momentum p_t as in [4]. For the low Q^2 sample the scattered positron was considered to be the cluster of maximum energy as at small p_t the fluctuations of the transverse momentum of the hadronic system become more pronounced. In both cases the electron identification was larger than 90% The cross section was calculated to be the same within 1-2% when the electron identification criterion was changed and the difference taken into account in the systematic error. The SPACAL cluster had to be associated with a signal in the preceeding drift chamber (BDC) and, if geometrically available, with a signal in the CIP, for the large Q^2 events, or with a track signature in the BST for the low Q^2 events. Utilizing the large signal-to-noise ratio of the silicon strip detectors, a BST track signature was accepted when a track segment could be built out of 2 hits in the acceptance region of 3 or 4 planes and this track was associated to the radial position of the selected cluster in SPACAL. For the determination of the event

z vertex position	$\|z\| < 30$cm
SPACAL cluster radius	< 4cm
SPACAL-BDC matching	$\delta r < 1.5$cm
electromagnetic SPACAL energy	> 3 GeV
hadronic SPACAL energy	$< 15\%$ of E'_e
total $E - p_z$	> 35 GeV

Table 1: *Basic criteria to select DIS events using the backward calorimeter and tracking system. Special cuts were made in the largest y region as discussed in Section 4.*

kinematics and background suppression a vertex had to be reconstructed in the CJC, CIP or BST.

The distributions of selected events were compared with simulations. Deep inelastic events were generated using the DJANGO [13] event generator. This program is based on HERACLES [14] for the electroweak interaction and on LEPTO [15] using the colour dipole model as implemented in ARIADNE [16] to simulate the hadronic final state. The DIS cross section was simulated according to a parametrization of the parton distributions [17] and setting $F_L = 0$. A reweighting procedure was applied using the QCD fit [4] and calculating F_L to NLO according to [18] for three light flavours and according to [19] for the charm contribution. Compton events were generated using the program COMPTON [20] and added to the Django Monte Carlo event sample. Photoproduction background was generated with the PHOJET [21] program. The detector response was simulated using the H1SIM program based on GEANT [22]. The simulated Monte Carlo events were subjected to the same reconstruction and analysis chain as the real data. For comparisons with experimental distributions the simulated spectra have been normalized to the measured luminosity.

The track reconstruction uses a set of drift chambers, proportional chambers and the BST which required careful alignment studies. These studies considered the variation of the z vertex position as well as the excentricity and inclination of the beam axis with respect to the H1 coordinate system. From a comparison of the polar angle measurements using BST tracks with the one obtained using the BDC and the event vertex, a systematic error of the polar angle measurement of 0.5 mrad was derived. The positron energy measurement in the highly granular SPACAL was calibrated using the double angle method and cross checked by the kinematic peak position at high energies (to 0.5% accuracy) and using Compton events at low energies (to 3% accuracy). The hadronic energy measurement in the LAr was calibrated imposing the p_t balance between the scattered positron and the hadronic final state particles. The energy scales of individual wheels and octants of the LAr calorimeter were determined using a global minimization technique which took into account the energy correlations. Where possible the calorimetric energy measurement has been replaced by the track momentum measurement and the associated calorimeter cluster was masked and excluded from the calculation of the total hadronic energy. The hadronic scale uncertainty is 4/3/5% for the contributions from LAr, tracks and the hadronic energy measurement in SPACAL, respectively.

A special calorimeter noise suppression has been performed in order to improve the structure function measurement at low y. Isolated cells with energies less than 400 MeV (800 MeV) in the central (forward) region of the LAr calorimeter were excluded from the analysis of both data and Monte Carlo events. This lead to a minimal signal loss but improved the y resolution at $y \sim 0.01$. Uncertainties in this subtraction procedure were included into the systematic errors.

The track detector efficiencies were determined from the data utilizing the redundancy of the central and backward tracking detector system and put into the simulation program. Very good agreement at the few per cent level was reached between experiment and simulation for the large set of technical and physics distributions studied. For example, Figure 1 shows distributions for the large Q^2 sample of data taken during the full 1997 running period. The experimental energy E'_e, angle θ_e, and the y_Σ and y_Σ/y_e distributions are well described by the event and detector simulation. Further control distributions for the high y region are shown in Section 4.

2.4 Cross Section Measurement

The cross section is determined by converting the measured number of events, after background subtraction, in a bin averaged cross section using acceptance calculations from the Monte Carlo sample. The data are binned in a grid in x and Q^2 as chosen previously [1]. The bin averaged cross section is corrected for first order radiative contributions with the program HERACLES [14]. Due to the $E - p_z$ cut, Table 1, the radiative corrections are small, even at large y. They were cross checked using the numerical program HECTOR [23]. A bin center correction was performed to obtain the differential cross section. The cross section data at large $y > 0.15$ are obtained using the reconstructed Q^2_e and y_e. At low $y < 0.15$, where the resolution of y_e degrades, the Σ variables Q^2_Σ and y_Σ are used. The results obtained with the two methods were found to be in excellent agreement down to lowest y which is strong evidence for the correct calibration of the SPACAL energy scale and resolution. All cross section data presented below were obtained in two independent analysis chains.

source	effect on cross section [%]
positron identification	0.5-2
vertex efficiency	1-2
BDC efficiency	0.5
BST efficiency	1-2
trigger efficiency	0.5 - 1
photoproduction background	< 8 at high y
radiative corrections	1-2
diffractive event simulation	2 at low Q^2, high y
noise rejection in LAr	< 3 at $y < 0.02$
track charge determination	1
charge asymmetry	1
CJC-SPACAL track link efficiency	2

Table 2: *Main sources of uncorrelated systematic errors and their effect on the cross section measurement accuracy. The resulting systematic errors are mostly below 4% extending up to 8% at the edges of the covered y range.*

Figure 2 presents the new data comparing the F_2 measurement with the previous structure function results of H1. The accuracy of this new, preliminary measurement surpasses all previous F_2 results obtained by H1. The new data are shown as solid points. They are in very good agreement with the 1994 (open points) and 1996 (open squares) data sets for the larger Q^2 region. Previous data at low Q^2 appear to be somewhat higher but are consistent with the data presented here within the quoted uncertainties. The main sources of uncorrelated systematic errors are summarized in Table 2. The cross section errors due to energy scale and polar angle measurement uncertainties, see Section 2.3, are treated as correlated error sources. Higher statistics and new instrumentation allowed the systematic uncertainties to be reduced to the level of 3-4% for the largest part of the kinematic region covered.

The striking rise of F_2 towards low x can be quantified by determining the exponent λ assuming $F_2 \propto x^{-\lambda}$ at fixed Q^2. Figure 3 illustrates the determination of λ using this data for $x < 0.1$ and $y < 0.6$. The determination of the λ exponent has reached an accuracy of 1% (statistical) and about 5% (systematic) for the intermediate Q^2 values.

3 QCD Analysis

3.1 Definitions

A NLO QCD fit to the cross section data was performed in the $\overline{MS}$ renormalization scheme using the DGLAP evolution equations for three light flavours with the charm contribution added according to the NLO calculation of the photon-gluon fusion process [19]. The input parton distributions at the starting scale Q_o^2 were parametrized as follows:

$$\begin{aligned} xg(x) &= A_g x^{B_g}(1-x)^{C_g}(1+D_g x+E_g\sqrt{x}), \\ xu_v(x) &= A_u x^{B_u}(1-x)^{C_u}(1+D_u x+E_u\sqrt{x}), \\ xd_v(x) &= A_d x^{B_d}(1-x)^{C_d}(1+D_d x+E_d\sqrt{x}), \\ xS(x) &= A_S x^{B_S}(1-x)^{C_S}(1+D_S x+E_S\sqrt{x}), \end{aligned} \tag{5}$$

where $S = \bar{u} = \bar{d} = 2\bar{s}$ defines the sea distributions [1]. The momentum sum rule was used to fix the normalization parameter A_S and the normalizations of the valence quark distributions were fixed by using the quark counting rules.

The fit was performed using an x space program developed inside the H1 collaboration [27]. The implementation of the NLO evolution formulae has been cross checked [28] to be in very good agreement with independent programs, one of them being written in moment space.

The QCD analysis program was extended to fit the inclusive reduced cross section, eq.4, and not only its $F_2(x,Q^2)$ part. This avoids the introduction of *ad hoc* assumptions on $F_L(x,Q^2)$ and allows data up to highest y to be included in the QCD analysis. The muon-proton and muon-deuteron DIS cross sections measured by the experiments BCDMS [29] and NMC [30] were also used to constrain the high x behaviour of the parton distributions. Target mass corrections were applied according to [31].

The starting point of the evolution was chosen to be $Q_o^2 = 2$ GeV^2 and data with $Q^2 \geq Q^2_{min} = 2$ GeV^2 were included in the fit. A cut was made to exclude BCDMS data in the region sensitive to higher twists ($x > 0.5$ for $Q^2 < 15$ GeV^2). For the fit values of $\alpha_s(M_Z^2) = 0.118$ and $m_c = 1.5$ GeV were chosen.

[1] This ansatz neglects the measured [24] difference of the $\bar{u}$ and $\bar{d}$ distributions. Using the parametrization of $\bar{u} - \bar{d}$ provided by [25] instead of assuming it to be zero has a negligible effect on the analyis subsequently presented. A possible difference [26] of s and $\bar{s}$ and the variation of the relative amount of strange sea have been checked to be of negligible influence on the result of the fit.

data set	Q^2 range	χ^2	change of normalization
H1 97	$2 \leq Q^2 \leq 10$	55/58	-
H1 97	$10 < Q^2 \leq 120$	106/80	-
H1 94-97	$120 < Q^2 \leq 30000$	130/108	-0.2 σ
NMC p	$2 \leq Q^2 < 100$	417/258	$\simeq$ -0.6 σ
NMC d	$2 \leq Q^2 < 100$	351/258	$\simeq$ -0.6 σ
BCDMS p	$7 < Q^2 \leq 250$	219/174	-1.4 σ
BCDMS d	$7 < Q^2 \leq 250$	215/159	-1.4 σ

Table 3: *Data sets used in the QCD cross section analysis, χ^2/number of points and change of normalization in units of normalization errors quoted by the experiments as required by the fit. The biggest renormalization is about -4% for the BCDMS data. The NMC data consists of 4 data sets corresponding to different muon beam energies. The p and d data sets were assumed to have a correlated normalization. The normalization of the present H1 data sets was fixed. In a fit with free normalizations the relative changes are of comparable size and the χ^2 is slightly better than in this fit.*

3.2 Results

In Figure 4 the QCD fit (solid line) is compared with the cross section data obtained in this measurement. The χ^2 is 1495 for 1095 data points using the uncorrelated errors of the measurements only. The χ^2 values of the different data sets are given in Table 3. The QCD fit enforced slight renormalizations of the measurements as listed in Table 3. The low x behaviour of $F_2(x, Q^2)$ is governed by the parameters B_g and B_S. These depend on Q_o^2 and come out to be equal to -0.18 and -0.14, respectively, for $Q_o^2 = 2$ GeV^2. In this fit the backward extrapolated gluon distribution at $Q^2 = 1$ GeV^2 becomes negative for $x < 0.01$ as has been observed also elsewhere [32].

At high y the cross section departs from the behaviour of F_2, dashed line in Figure 4. This departue is due to the longitudinal structure function differing significantly from zero. A detailed analysis of the high y data and of F_L is presented in Section 4.

The fit presented in Figure 4 included the preliminary H1 cross section data measured at high $Q^2 > 120$ GeV^2 which are very well described. In order to check the predictive power of QCD and the consistency of the two data sets, the cross section fit was repeated excluding the high Q^2 data from the minimization. This leads to a nearly indistinguishable QCD cross section. Thus within the presently reached accuracy of the high Q^2 data, the Q^2 behaviour of the cross section appears to be predictable within NLO QCD over two orders of magnitude of Q^2, from $Q^2 \simeq 200$ GeV^2 to $Q^2 \simeq 20000$ GeV^2, using the DIS cross section measurements restricted to $Q^2 < 200$ GeV^2. The high Q^2 H1 analysis identifies the scattered positron in the central and forward LAr calorimeter while the low Q^2 data analysis uses the backward SPACAL with different tracking detectors for positron track reconstruction. Experimentally it is important to notice that the data obtained in independent analyses and using different parts of the H1 detector for reconstruction of the scattered positron are in very good agreement.

In Figures 5 and 6 detailed comparisons are made of the Q^2 dependence of the low Q^2 data of H1 and the BCDMS and NMC experiments with the QCD cross section obtained in the fit. It is seen that the H1 data for $x < 0.01$ are approaching the few % level of precision reached by the fixed target experiments. The scaling violations are well described by the NLO QCD fit over five orders of magnitude in x, from $x = 5 \cdot 10^{-5}$ to $x = 0.65$. The quality of the data is a challenge to its theoretical analysis.

A QCD fit was also performed to the structure function data restricted to $y < 0.35$ in order to be independent of F_L. This fit is compared in Figure 7 with the new data on F_2. The description of the measurement is impressive. It is interesting to notice that this fit and the cross section fit give results for F_2 and F_L which agree within 1% at lowest x for the Q^2 region of this data. Thus the gluon distribution is fixed by the Q^2 dependence of F_2 at lower y and the influence of F_L on the fit result is small given the presently reached accuracy of the high y cross section measurement.

4 Cross Section Measurement at Very Large y

4.1 Data Analysis

The measurement of the DIS cross section at HERA at high y requires the positron of a few GeV of energy to be identified and the large background from photoproduction processes to be removed. Since the main part of the background is due to $\pi_0 \rightarrow \gamma\gamma$ decays the low energy background is removed to a large extent by requiring a track pointing to the cluster reconstructed in the SPACAL. At large Q^2 this track is identified with a valid hit pattern in the inner proportional chamber CIP and, for $10 < Q^2 < 40$ GeV^2, as a momentum measured track in the CJC which for energies below 15 GeV has an identified charge. This has been described in detail in [4] and further investigations have been performed. The tagged background is found to be charge symmetric within the statistical accuracy of 4%, see Figure 8. From a study of double tracks with opposite charge in the whole background sample it was found that a large part of the background is due to conversion of photons. Based on these observations and the simulation of photoproduction background, charge symmetry is assumed to hold within 3%. Some control distributions are shown in Figure 8 which illustrate the good understanding of the region of extremely high y extending to $E'_e = 3$ GeV.

In the low Q^2 region the high y range was accessed by requiring a track signal in the BST. The largest y cross section data quoted here were obtained in a dedicated analysis which used only the SPACAL and the BST with a minimum bias trigger of 5 GeV threshold. Here the vertex position has been taken only from the positron track candidate passing the BST and the polar angle measurement of the silicon tracker was used. This analysis was performed for the whole acceptance region of the BST and found to be in good agreement with the more standard analysis. Figure 9 shows the polar angle distribuion, the high y part of the energy spectrum and the energy distribution measured in the electron tagger. The distributions agree very well with simulations.

All cross sections measured at high y are given in Figure 4. For comparison with previous measurements the data for Q^2 between 12 GeV^2 and 35 GeV^2 are displayed also in Figure 10. The measurements at high y are seen to be consistent and some local deficiencies of the preliminary 1996 data at lower y became understood. The measured cross sections reveal a departure from the behaviour of F_2 (dashed line) at high y which can be attributed to F_L differing from zero, see below.

4.2 Cross Section Derivative $\partial\sigma_r/\partial\log y$

The cross sections were used to measure the derivative $\partial\sigma_r/\partial\log y$ at fixed Q^2 in the whole y range accessible. This derivative is defined as:

$$\frac{\partial\sigma_r}{\partial\log y} = -\frac{\partial F_2}{\partial\log x} - F_L\cdot 2y^2\cdot\frac{2-y}{Y_+^2} + \frac{\partial F_L}{\partial\log x}\cdot\frac{y^2}{Y_+}. \tag{6}$$

The data were binned in y and differences $\Delta\sigma_r$ were calculated between all cross section points adjacent in y. A bin center correction was applied to obtain the derivative $\partial\sigma_r/\partial\log y$ at each y point determined as the average of the two y values involved. Contrary to a standard representation of the data where systematic errors introduce positive correlations between neighbouring points, the two adjacent measurements of $\partial\sigma_r/\partial\log y$ anticorrelate since they contain the same cross section measurement with different sign. Due to the subtraction the systematic errors cancel to a large extent apart from those with a pronounced dependence on y as the photoproduction background at high y and the LAr noise treatment at low y, for example. On the contrary the statistical errors are sizeable which required the derivative data to be presented in coarser Q^2 bins than the cross section measurement.

In Figure 11 the cross section derivative measurement is compared with the NLO QCD calculation using different assumptions on F_L. The derivative is seen to be very sensitive to the longitudinal structure function. This is due to the direct occurence of F_L in the derivative of σ_r, Eq. 6. For $y\to 1$ the cross section derivative tends to the limit $-\partial F_2/\partial\log x\ -\ 2\cdot F_L$ with a negligible contribution from the derivative of F_L. This is in contrast to the F_L influence on the non-differentiated cross section σ_r, see Figure 10, where the contribution of F_2 dominates for all y and thus has to be controlled with high precision.

4.3 Longitudinal Structure Function

The measurement of $\partial\sigma_r/\partial\log y$ can be used to determine the longitudinal structure function in a new way. In the former method, introduced in [2], an assumption has to be made on the value of F_2 at large y. In the new method one has to control the cross section derivative which at fixed Q^2 requires to control the slope of F_2 with x. Furthermore the effect of F_L on the measured quantity, relatively to the F_2 part, is larger in the case of the cross section derivative than in the cross section itself. In the analysis the assumption has been made that the derivative $\partial F_2/\partial\log y$ is a linear function of $\log y$ up to large y. For all Q^2 straight line fits were made to the derivative data for $y < 0.2$ which describe the data very well. The extrapolation of a straight line was taken to represent the contribution of F_2 at high y. The extrapolations were compared with the values obtained from QCD and very good agreement was found. The uncertainties of the straight line extrapolation were included into the systematic errors of the measurement. The small contribution of $\partial F_L/\partial\log y$ to the derivative was corrected for by using NLO QCD and the full correction was added to the overall error of the measured F_L. This method can also be applied at fixed x instead of Q^2. In this case one has to understand the behaviour of $\partial F_2/\partial\log Q^2$.

This procedure leads to new values of F_L (Figure 12) which are consistent with former measurements [2,4]. Good agreement is seen with the F_L values derived using the method introduced previously [2], closed points. Both methods use the same data. Yet, the uncertainties of the determined F_L are by construction different. Since at low Q^2 the extrapolation using QCD is uncertain, F_L values down to $Q^2 = 3$ GeV^2 are quoted only using the derivative method. Note that the systematic errors of the $F_L(x, Q^2)$ points are largely correlated as the systematic errors are mainly a function of y in comparable Q^2 intervals. In the derivative method the results at the two y values are correlated. The points belonging to the larger y bin have a sizeable statistical error due to the specific trigger and background subtraction procedure used in this region.

In Figure 12 the band is drawn which represents the small uncertainty of the calculation of F_L using the gluon and quark distributions, as determined from the NLO QCD fit to F_2 described above. The data are consistent with this calculation.

5 Summary

A new, preliminary measurement of the deep inelastic positron-proton scattering cross section has been presented based on data taken by the H1 Collaboration at HERA running with positrons of 27.5 GeV energy and with protons of 820 GeV energy. The data comprises two samples of events: a sample of 15 pb^{-1} at large momentum transfers ($10 < Q^2 \leq 120$ GeV^2), collected during the whole 1997 running period, and a sample of 2 pb^{-1} at low momentum transfers ($2 \leq Q^2 < 10$ GeV^2) taken in a dedicated run in the fall of 1997.

The statistical accuracy of the measured inclusive cross sections is better than 1% for a large part of the data. The systematic precision has reached the level of 3-4% apart from the edges of the covered range. Improvements were due to the higher statistics allowing more refined systematics studies to be performed, and due to new instrumentation with the backward silicon tracker for the measurement of low Q^2 scattering.

These data represent thus the so far most precise measurement of the proton structure function $F_2(x, Q^2)$ by H1. It is in agreement with previous results within the quoted systematic accuracy which is now comparable with the precision of fixed target lepton-proton scattering experiments.

The cross section data was analyzed in NLO QCD with three light flavours and the heavy quark contribution was added according to boson-gluon fusion NLO calculations. The data is well described by the QCD analysis over the whole range of x from $3 \cdot 10^{-5}$ to 0.13. This analysis included the data obtained by H1 at even higher Q^2 and by the NMC and BCDMS experiments. These data sets appear to be in very good agreement.

The measurement of the cross section at large Q^2 was extended to minimum energies of the scattered positron of 3 GeV. The use of the silicon tracker permitted to access the low Q^2, high $y < 0.75$ region with improved precision. This lead to new measurements of the DIS cross section at high y where it is sensitive to the longitudinal structure function $F_L(x, Q^2)$.

A novel method has been introduced to access with improved sensitivity the F_L part of the cross section by measuring the derivative $\partial\sigma_r/\partial\log y$ of the reduced cross section at fixed Q^2. This method profits from a cancellation of systematic errors and has been used to extract $F_L(x,Q^2)$ down to $Q^2=3$ GeV^2. The values of the longitudinal structure function presented here are in good agreement with previous results and consistent with F_L as calculated in the NLO QCD analysis.

Acknowledgements We are very grateful to the HERA machine group whose outstanding efforts made this experiment possible. We acknowledge the support of the DESY technical staff. We appreciate the substantial effort of the engineers and technicians who constructed and maintain the detector. We thank the funding agencies for financial support of this experiment. We wish to thank the DESY directorate for the support and hospitality extended to the non-DESY members of the collaboration. Finally we thank J. Blümlein, W. van Neerven and A. Vogt for interesting discussions on the theoretical interpretation of this result.

References

[1] H1 Collaboration, S. Aid et al., Nucl. Phys. **B 470** (1996) 3.

[2] H1 Collaboration, S. Aid et al., Phys. Lett. **B 393** (1997) 452.

[3] H1 Collaboration, C. Adloff et al., Nucl. Phys. **B 497** (1997) 3.

[4] H1 Collaboration, "A measurement of the inclusive deep inelastic scattering cross section at low Q^2 at HERA", submitted to the International Europhysics Conference on High Energy Physics, Jerusalem, Israel, Paper 260, 1997, unpublished.

[5] H1 Collaboration, "Measurement of neutral and charged current cross-sections at high Q^2", submitted to the XXIXth International Conference on High Energy Physics, Vancouver, Canada, Paper 533, 1998, unpublished.

[6] A. Blondel and F. Jaquet, Proc. ep Facility for Europe, Amsterdam 1979, DESY 79/48 (1979) 391.

[7] U. Bassler and G. Bernardi, Nucl. Instr. Meth. **A361** (1995) 197.

[8] M. Klein and T. Riemann, Z.Phys. **C24** (1984) 151.

[9] H1 Collaboration, I. Abt et al., Nucl. Instr. and Meth. **A386** (1997) 310 and **A386** (1997) 348.

[10] R. Appuhn et al., Nucl. Instr. and Meth. **A 386** (1997) 397.

[11] W. Eick et al., Nucl. Instr. and Meth. **A386** (1997) 81.

[12] H1 Collaboration, I.Abt et al., Z.Phys.**C66** (1995) 529.

[13] G. A. Schuler and H. Spiesberger, Proceedings of the Workshop on HERA Physics, Vol 3, eds. W. Buchmüller and G. Ingelman, Hamburg, DESY (1992), p. 1419.

[14] A. Kwiatkowski, H. Spiesberger and H.-J. Möhring, Computer Phys. Comm. **69** (1992) 155.

[15] G. Ingelman, Proceedings of the Workshop on HERA Physics, Vol 3, eds. W. Buchmüller and G. Ingelman, Hamburg, DESY (1992), p. 1366.

[16] L. Lönnblad, Comp.Phys.Comm. **71**(1992)15.

[17] M. Glück, E.Reya and A.Vogt, Z. Phys. **C 67** (1995) 433.

[18] E.B. Zijlstra and W. van Neerven, Nucl. Phys. **B 383** (1992) 525;
S.A. Larin and J.A.M. Vermaseren, Z Phys. **C 57** (1993) 93.

[19] E. Laenen et al., Nucl. Phys. **B 392** (1993) 162.
S. Riemersma, J. Smith and W. van Neerven, Phys. Lett. **B 347** (1995) 143.

[20] A. Courau and P. Kessler, Phys. Rev. **D 46** (1992) 117.

[21] R. Engel and J. Ranft, Phys. Rev. **D 54** (1996) 4244.

[22] R. Brun et al., GEANT3 User's Guide, CERN-DD/EE 84-1, Geneva (1987).

[23] A. Arbuzov et al., Comput. Phys. Comm. **94** (1996) 128.

[24] E866/NuSea Collaboration, E. A. Hawker et al., Phys. Rev. Lett. **80** (1998) 3715;
HERMES collaboration, DESY 98-078, hep-ex/9807013, submitted to Physical Review Letters.

[25] A.D. Martin et al., DTP/98/10, RAL-TR-98-029 (1998).

[26] F. Zomer, Talk presented at the International Workshop on Low x Physics, Zeuthen, April 1998, unpublished.

[27] C. Pascaud and F. Zomer, LAL preprint, LAL/95-05 (1995).

[28] J. Blümlein et al., Proceedings of the Workshop on HERA Physics, Vol.1, eds. G. Ingelman, A De Roeck and R. Klanner, Hamburg, DESY (1996), p.23.

[29] BCDMS Collaboration, A.C. Benvenuti et al., Phys. Lett. **B223** (1989) 485;
CERN preprint CERN-EP/89-06. Note that the analysis was performed using the data set as modified by M. Virchaux and A. Milzstajn (Phys. Lett. **B274** (1992) 221) to account for systematic effects.

[30] NMC Collaboration, M. Arneodo et al., Nucl. Phys. **B483** (1997) 3.

[31] H. Georgi and H.D. Politzer, Phys. Rev. **D 14** (1976) 1829.

[32] M. Botje, Contribution to the Workshop on Deep Inelastic Scattering at Low x, Zeuthen, April 1998, unpublished.

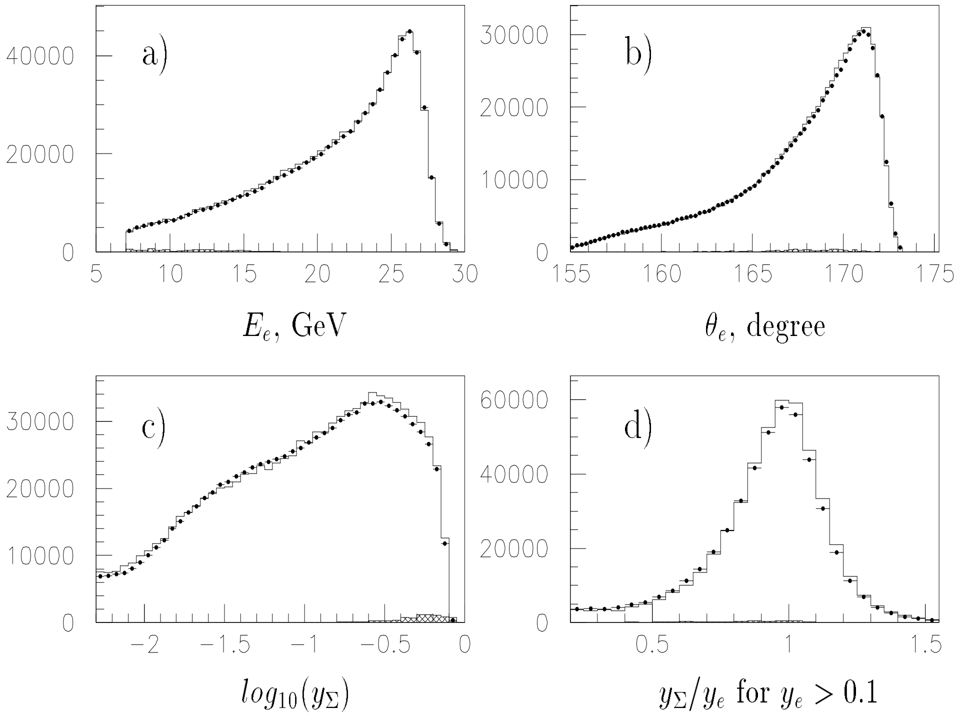

Figure 1: Distributions of the energy and of the polar angle of the scattered positron, of y_Σ and of the ratio y_Σ/y_e for the large Q^2 data sample taken in 1997. The histograms are a sum of the DIS event simulation and the small contribution from the simulated background due to photoproduction (hatched). The simulated spectra are normalized to the luminosity of the data.

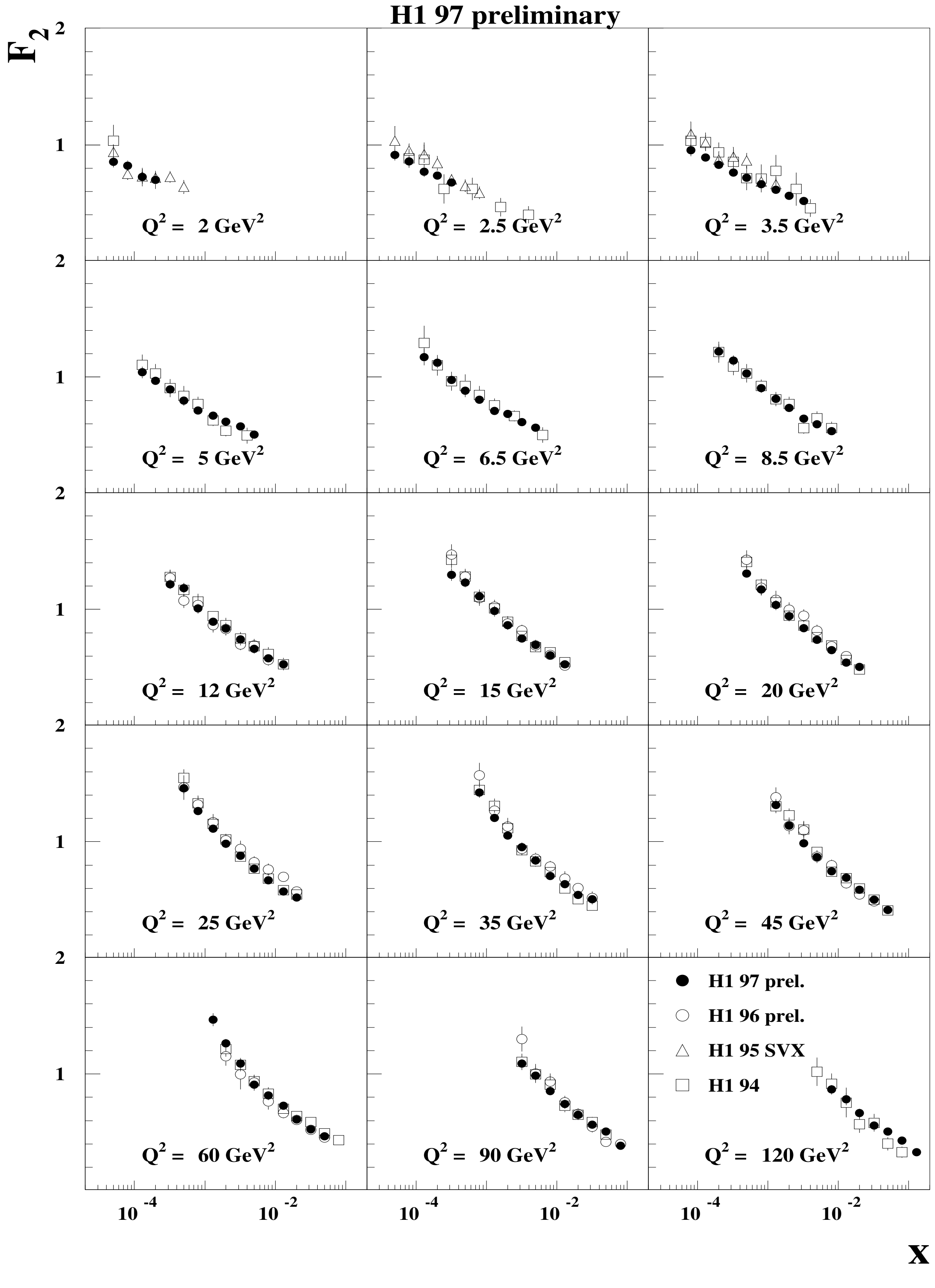

Figure 2: Measurements of the proton structure function F_2 by the H1 experiment for $y < 0.6$: solid points: this measurement, run 1997; open squares: published 1994 data obtained with a different backward apparatus [1]; open triangles: published data [3] from the 1995 run with shifted vertex position; open points: preliminary data [4] from the 1996 run. The previous F_2 values were calculated using for F_L a parametrization based on [17]. This leads to slightly larger F_2 values at high y than the QCD fit parametrization of F_L.

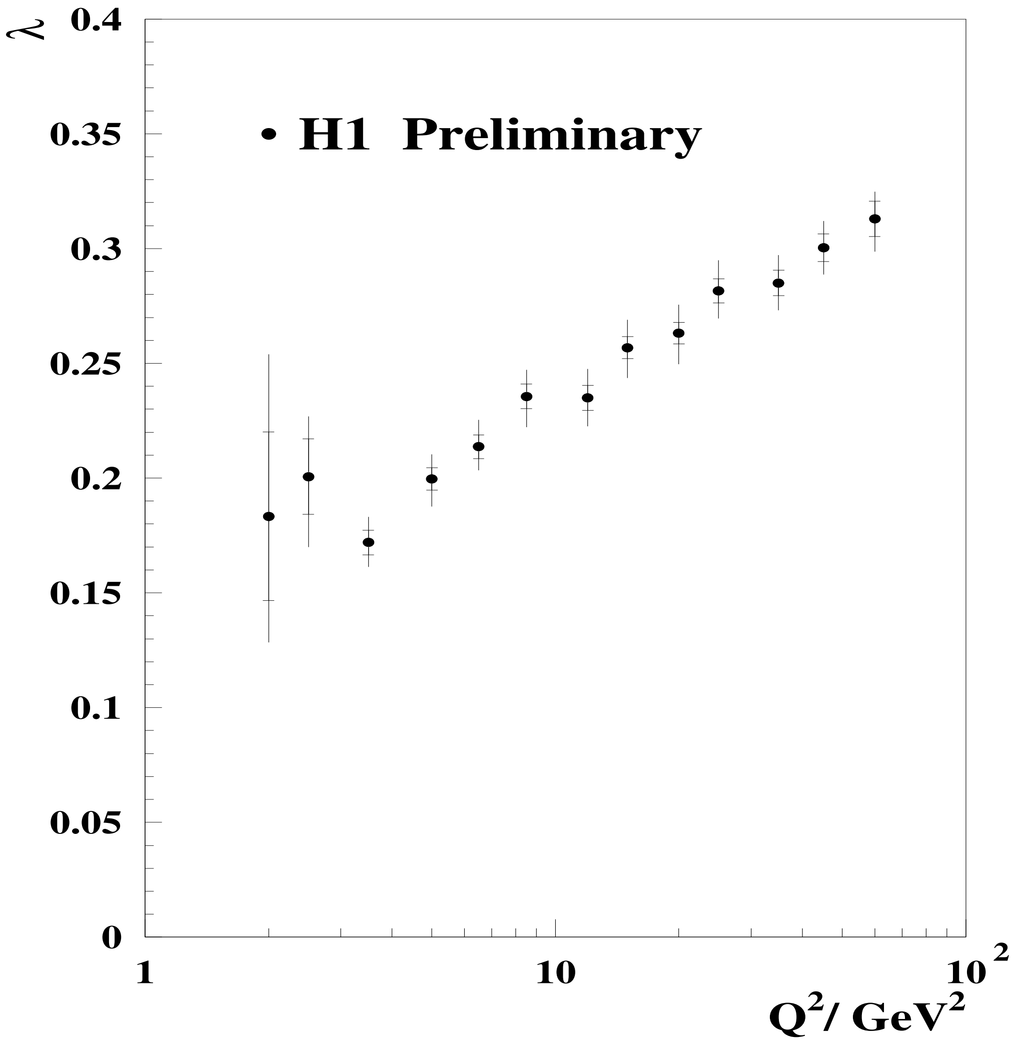

Figure 3: Determination of the parameter λ describing for fixed Q^2 the rise of F_2 towards low x assuming that $F_2 \propto x^{-\lambda}$ and restricting x to values < 0.1 where approximately F_2 changes its shape. The inner error bar is the statistical error, the outer error bar represents the total uncertainty.

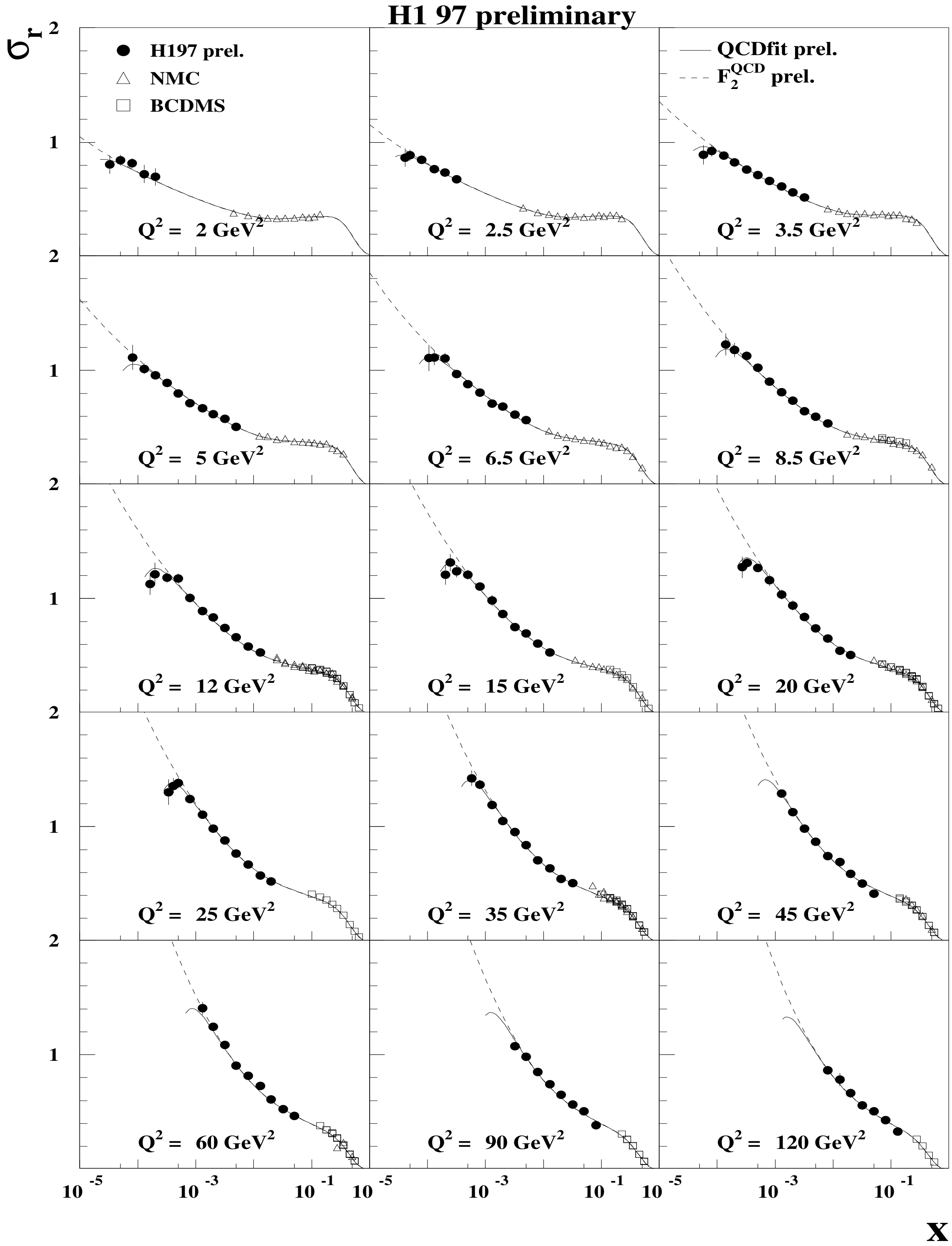

Figure 4: Measurement of the reduced DIS scattering cross section, eq.4, closed points. Triangles (squares) represent data by the NMC (BCDMS) muon proton experiments. The fit is a NLO QCD fit to the H1, the NMC and BCDMS proton and deuteron cross section data as described in the text. The dashed curve is the F_2 structure function determined with this fit. At lowest x, corresponding to large $y \geq 0.5$, departures of the cross section from the rise of F_2 towards low x occur which are due to F_L differing from zero.

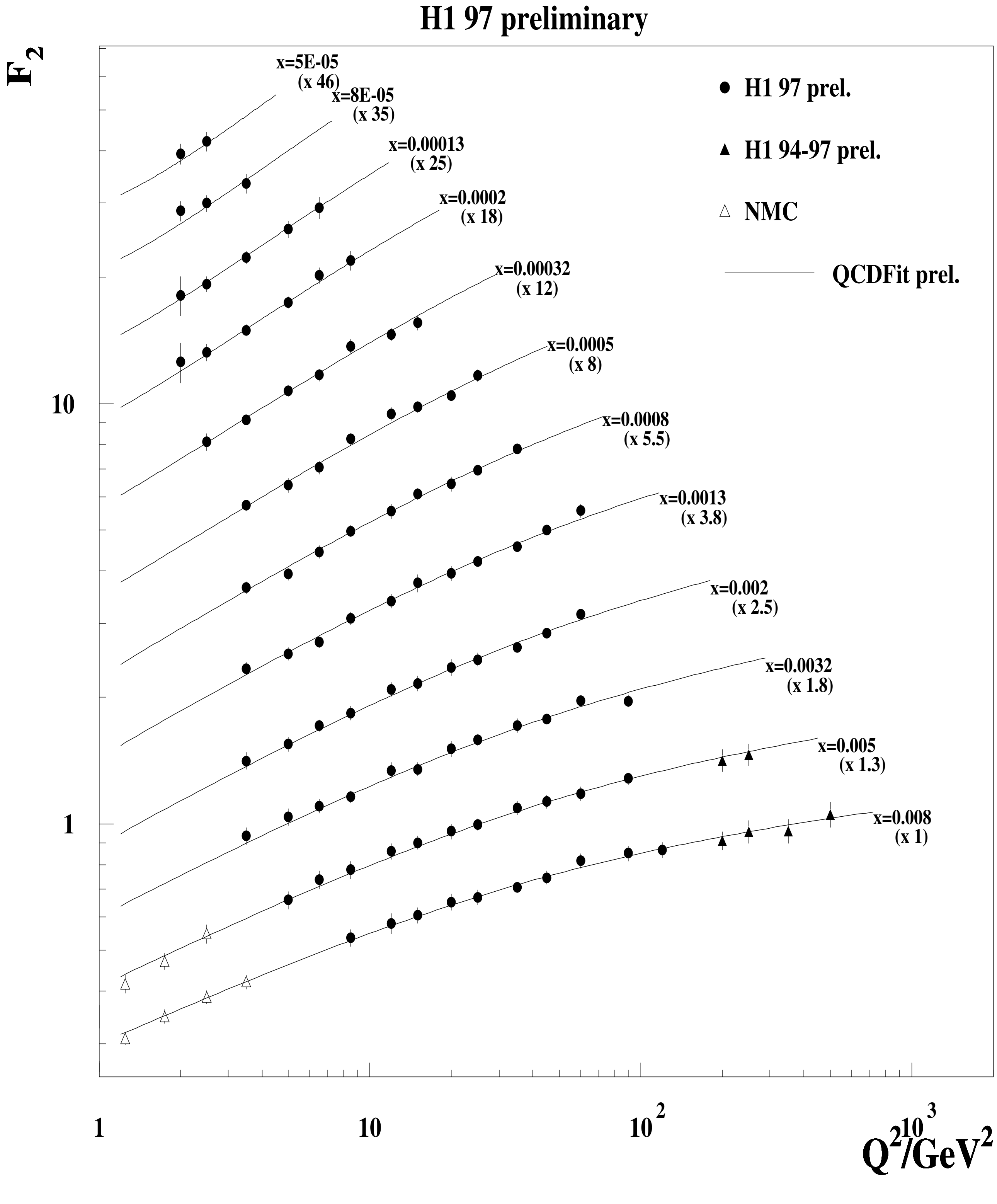

Figure 5: Structure function measurements by H1 ($y < 0.6$), and the NMC experiment. Solid line: NLO QCD fit to the H1, NMC and BCDMS cross section data.

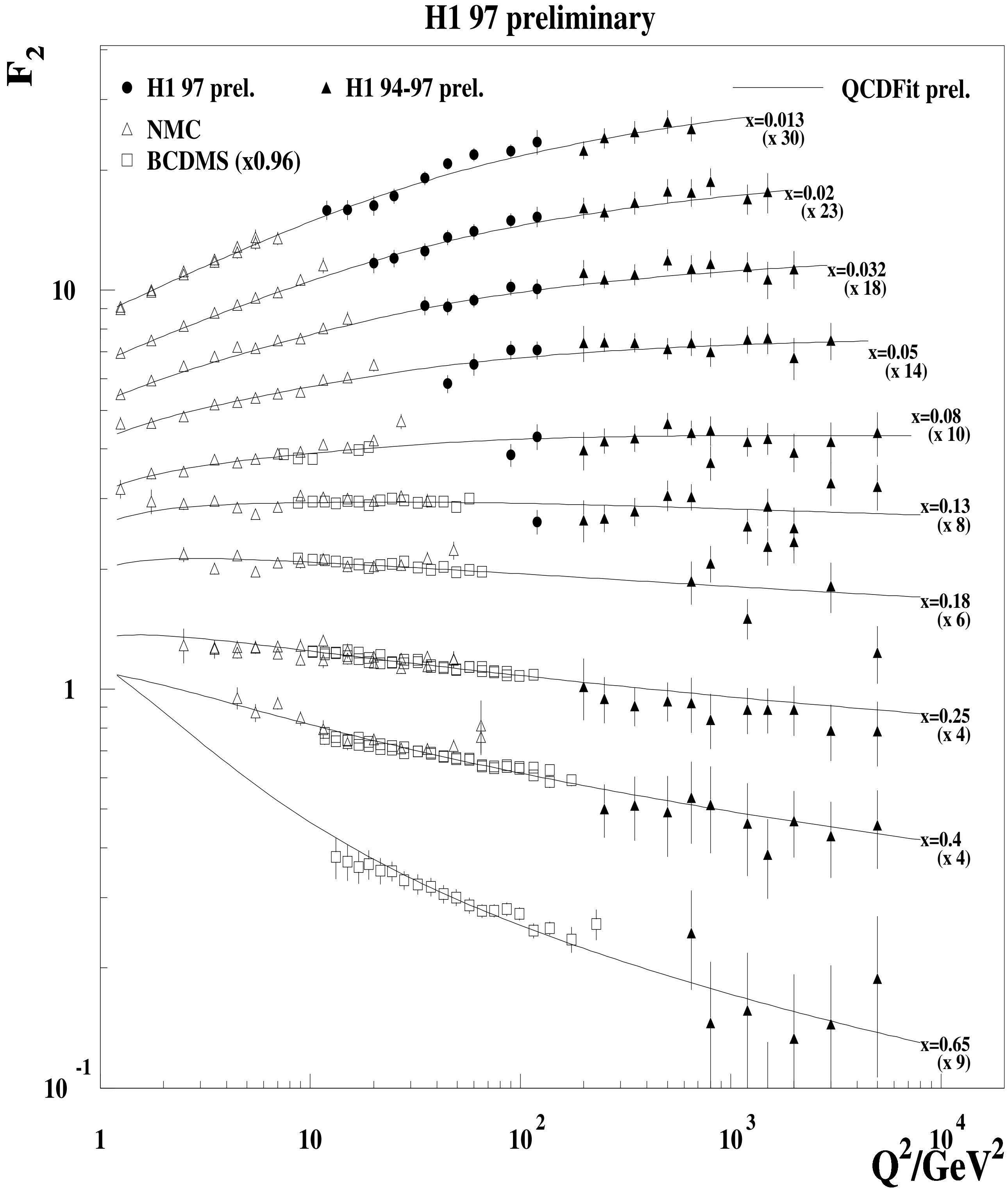

Figure 6: Structure function measurements by H1 ($y < 0.6$), NMC and BCDMS as used in the NLO QCD analysis (solid line). The H1 data (triangles) at $Q^2 > 150$ GeV^2 is due to the measurement [5] using the LAr calorimeter for positron detection. It is shown here up to $Q^2 < 5000$ GeV^2. The BCDMS data are downscaled by 4% as required by the QCD fit.

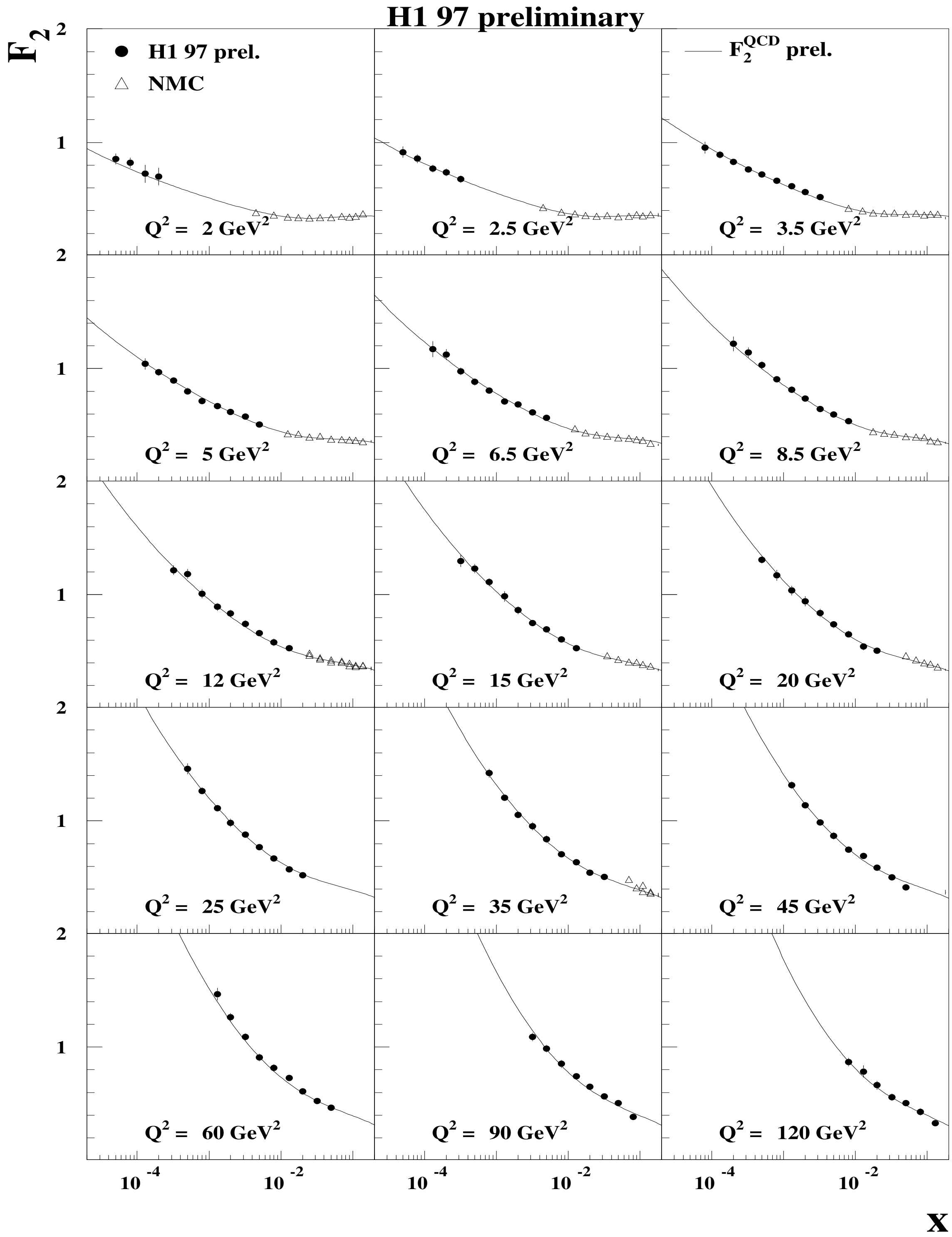

Figure 7: Measurement of the proton structure function F_2 compared with the NLO QCD fit to the H1, NMC and BCDMS data. The maximum y values included are < 0.6. F_2 has been obtained from the measured cross section by using F_L as calculated using the NLO QCD fit.

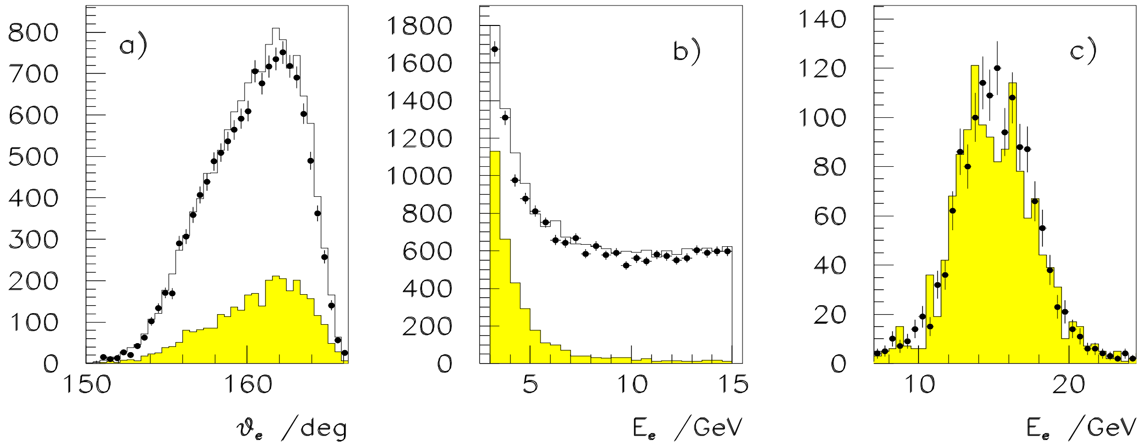

Figure 8: Distributions illustrating the cross section measurement at high y and large Q^2 where the central drift chamber is used to measure tracks linked to a low energy cluster reconstructed in SPACAL: a) polar angle and b) SPACAL energy distributions before subtraction of the residual photoproduction background using the charge measurement by the CJC. Solid points: data with positive charge assignment. Dashed histogram: data with negative charge assignment. Open histogram: superposition of data with negative charge assignment and DIS event simulation, normalized to the data luminosity. c) Spectrum of energy measured in the electron tagger for DIS candidate events with a track of positive (solid points) and negative charge (histogram).

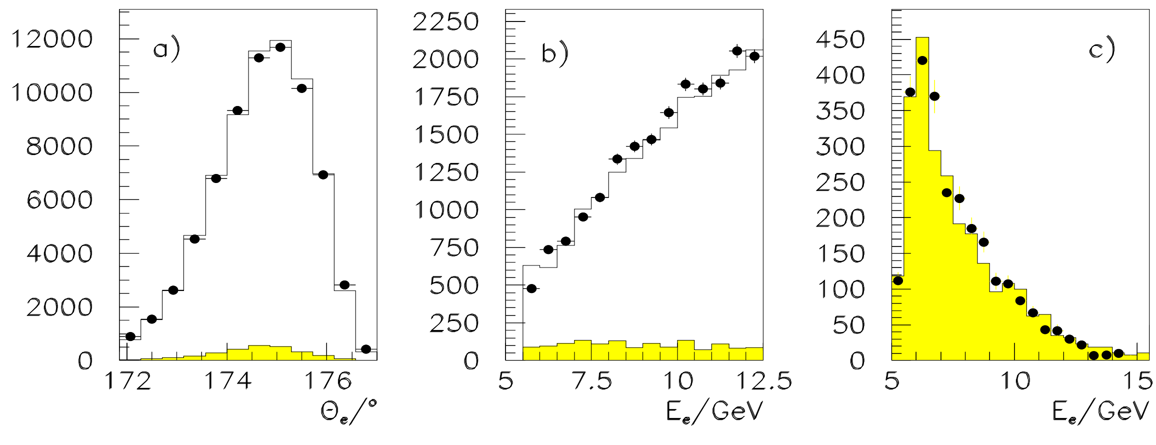

Figure 9: Distributions obtained in a dedicated analysis of data taken during the 1997 minimum bias run. This analysis uses only the BST and the SPACAL. Distributions of the polar angle (a) and of the energy (b) of the scattered positron candidate as measured in SPACAL for $1.8 < Q^2 < 5$ GeV^2. Open histogram: Simulation of DIS and photoproduction events (hatched). c) SPACAL energy spectrum for events in the BST acceptance with an electron tagged downstream. Closed points: H1 data, histogram: simulation of photoproduction events.

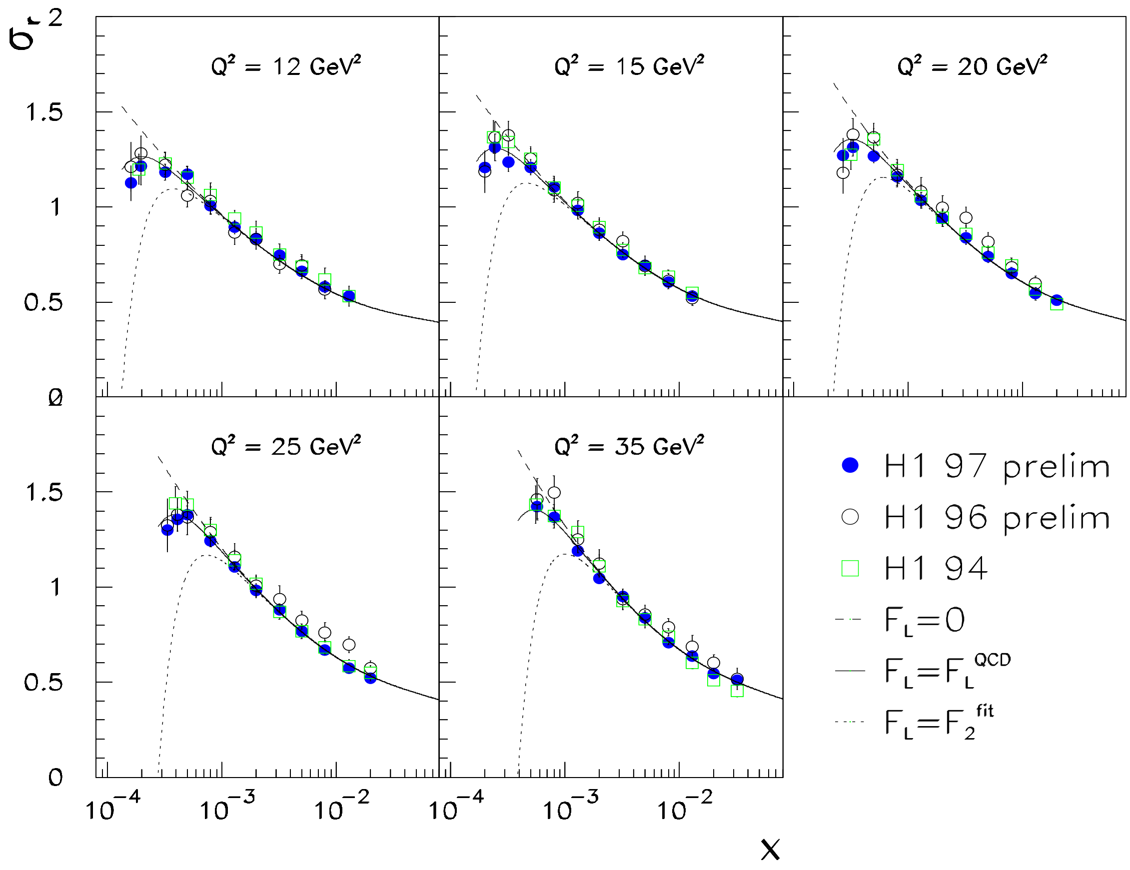

Figure 10: Measurement of the reduced DIS cross section, eq.4. Closed points: this measurement. Open squares: H1 data from the 1994 run [2] taken with a different backward setup. Open points: H1 data from the 1996 run [4]. The central y values extend to 0.82. The curves represent cross sections derived from the NLO QCD fit to the present F_2 data including only data for $y < 0.35$. This F_2 is extrapolated to large y values (giving the cross section for $F_L = 0$, dashed curve), and the cross section is calculated using the F_L determined by the NLO QCD fit (solid curve) and assuming F_L to be equal to F_2 (dotted curve).

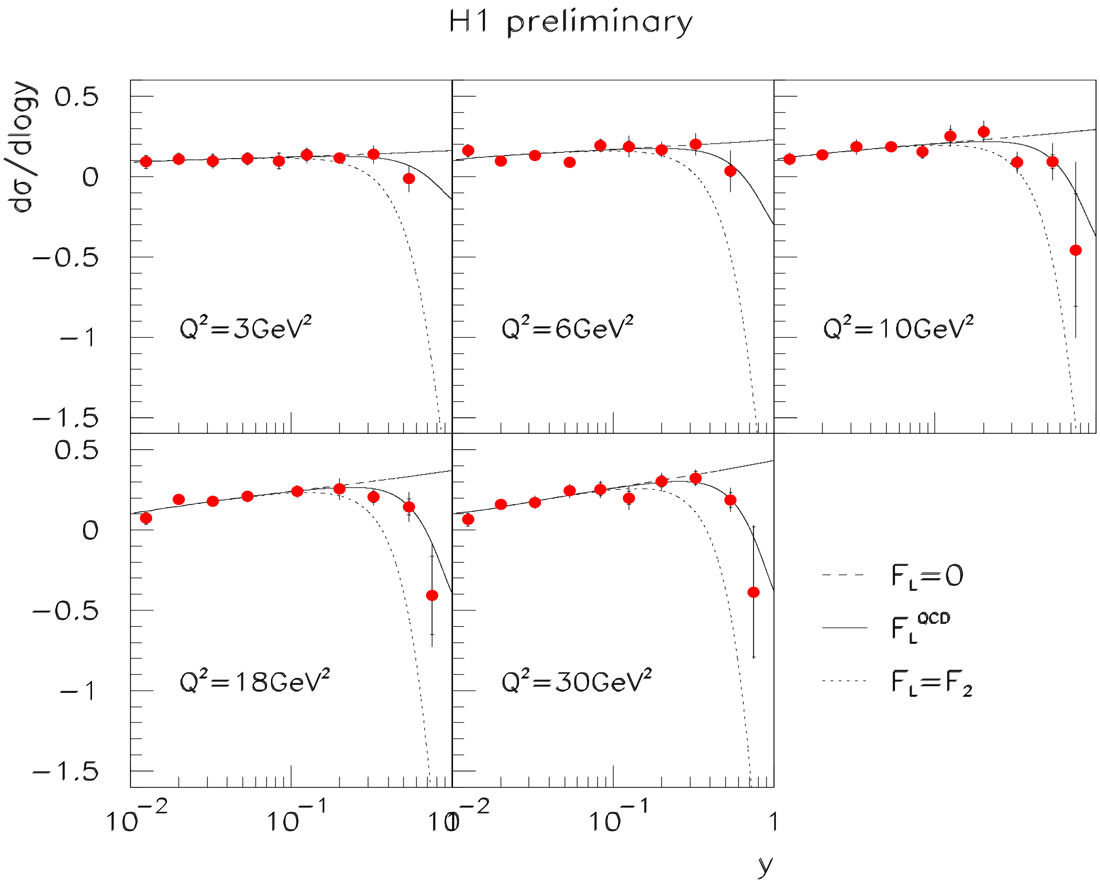

Figure 11: Measurement of the derivative $\partial\sigma_r/\partial \log y$. The curves represent the QCD cross section fit replacing the F_L fit result (solid curve) by $F_L = 0$ (dashed curve) and by $F_L = F_2$ (dotted curve). The inner error bar is the statistical error and the total error bar denotes the statistical and systematic errors added in quadrature.

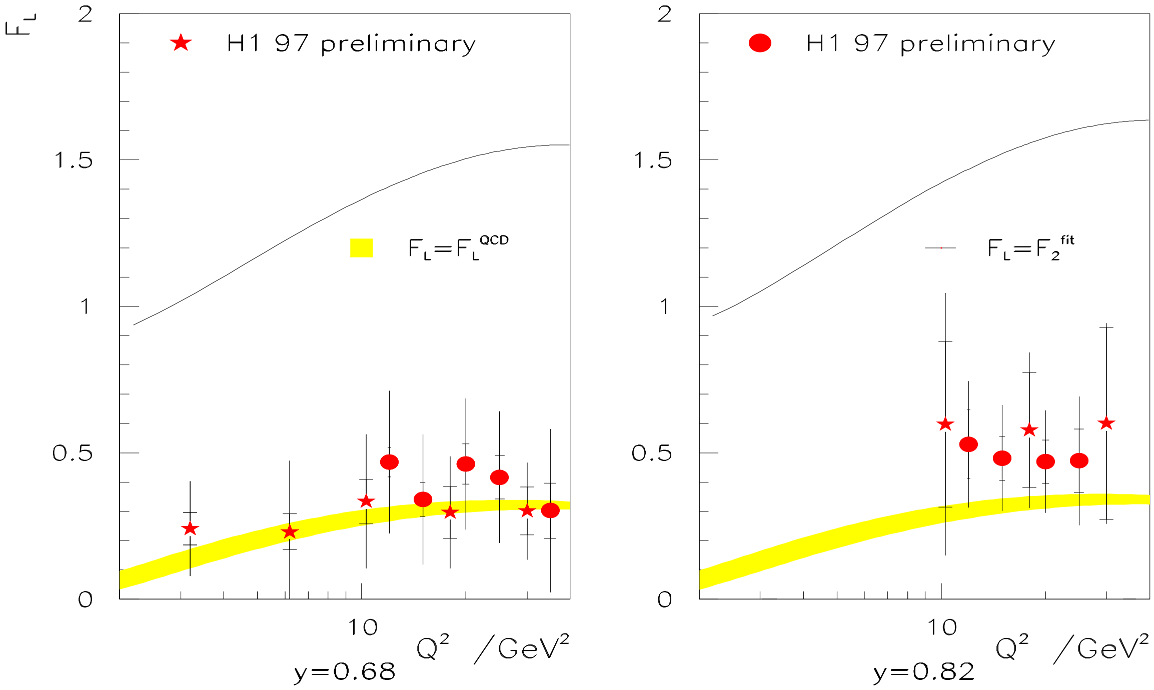

Figure 12: Determination of the longitudinal structure function F_L using the method as introduced in [2] (closed points) and the derivative method (stars) which extends to lower Q^2. The quoted y values apply to the closed points. The stars belong to somewhat lower y values as they are derived from a difference of cross section measurements. The two determinations use the same data set. The narrow band represents the uncertainty range of F_L when calculated using the gluon and quark distributions determined with the NLO QCD fit to the H1, NMC and BCDMS data.